ORIGINAL ARTICLE

Development and performance evaluation of sustainable lightweight geopolymer based fireproofing coatings for steel construction

Zhenyu Huang[a,b*], Yingwu Zhou[a,b], Hammad Salahuddin[a,b]

[a] Guangdong Provincial Key Laboratory of Durability for Marine Civil Engineering, Shenzhen University, Shenzhen, China 518060.
[b] College of Civil and Transportation Engineering, Shenzhen University, Shenzhen, China 518060.
*Corresponding Author: Zhenyu Huang. Email address: huangzhenyu@szu.edu.cn.

Abstract: This study developed a novel, sustainable, lightweight, and high-ductility fireproofing coating using granulated blast furnace slag (GBFS), fly ash microspheres (FAC), alkali activator, and polyethylene (PE) fiber as raw materials. The critical mixing ratios of FAC to GBFS (4:6), the water-to-binder ratio (0.55), and the alkali activator modulus (1.4) were determined to meet the requirements for fluidity, compressive strength, and flexural strength. The residual strength and thermal stability of the sample were evaluated through high-temperature exposure tests. The compressive strength results showed that even at 900℃, the lightweight geopolymer-based fireproofing coating exhibited 23 MPa as compared to that of 61 MPa at room temperature, which is 30% of its room temperature strength. X-ray diffraction and scanning electron microscopy were carried out to examine the micro-morphology of the samples, revealing that the main component of the geopolymer was $Ca_2(Al_2SiO_7)$ in a colloidal state at 30℃, 300℃, and 600℃. The reduction in strength at this temperature range was mainly attributed to the surface crack extension. However, at 900℃, the gelatinous $Ca_2(Al_2SiO_7)$ underwent dehydration and transformed into crystalline $Ca_2(Al_2SiO_7)$, or zeolite. The interface bond performance between the fireproofing coating and the steel plate was thoroughly tested through direct shear and normal bond tests, using five different bonding techniques, as well as a tensile test on the fire-resistant material coated steel plate. The bond strength from direct shear test ranged from 0.05 MPa to 1.64 MPa and for normal shear test, the strength was in the range of 0.07 MPa to 1.43 MPa. The results of tensile strength test showed that the coating had high ductility and was fire-resistant, and it could deform synergistically with the steel plate, with a maximum tensile strain of 4%. These results demonstrate the coating's excellent deformation performance.

Keywords: Geopolymer; fireproofing coating; Mixing ratio; Fire-resistance; Ductility; Sustainable materials.

1 Introduction

Fire is a major safety hazard and challenge for building structures, causing significant property losses and casualties each year. With the high density of urban populations, high-rise buildings are becoming increasingly common, and in the event of a fire, they pose a significant threat to human safety and property. To prevent fires or slow down their spread, extensive research has been done to develop fire protection facilities and fire-resistant materials for high-rise buildings [1–3]. For building

construction, steel and reinforced concrete are widely used materials. Steel provides higher tensile strength and better ductility and seismic performance compared to concrete. The fast-track construction of prefabricated steel structures also provides ample developmental space for buildings [4–6]. However, steel has a disadvantage in terms of its low fire resistance. Without fireproof protection, steel can heat up quickly, causing it to partially or completely lose its strength, potentially leading to the collapse of the entire building. Improving the fire resistance of steel structures is crucial to facilitate its wider application, and the use of fireproof coatings is a promising solution. Currently, commercially available fireproof coatings for steel structures can be classified into two categories: organic and inorganic materials. Organic materials tend to decompose and release toxic gases at high temperatures, resulting in a limited fire resistance time. Inorganic concrete, on the other hand, is a thermally inert material with a long fire resistance time but also a significant self-weight. The bond between steel plates and concrete is also limited, making it susceptible to separation under stress.

As a novel type of cementitious material, geopolymer is typically made from silicoaluminous materials and produced using an alkaline activator [7,8]. It has several advantages, such as high heat resistance [9], strength, durability, low production costs, energy consumption, and CO_2 emissions [10]. Many studies have also found promising performance of geopolymer materials against corrosion, which is very important feature for a fireproofing coating material for steel structures [11–15] . These desirable properties make geopolymer a potential fire-resistant material [16]. However, there are also drawbacks to its use, such as high density, thermal conductivity, and poor ductility [17–20]. Numerous studies have been conducted on the mechanical and thermal properties and applications of geopolymer, including bond performance of geopolymer materials with fiber reinforced polymer bars [21]. Temuujin et al.[22] investigated the feasibility of using fly ash to produce geopolymer fireproof coatings on metal substrates. They altered the Si:Al ratio and water-binder ratio and analyzed the composition, microscopic morphology, thermal expansion and shrinkage behavior of geopolymers with different compositions. The results showed that the adhesion strength of the coating to steel was determined by its chemical composition, with the highest adhesion strength (over 3.5 MPa) obtained for highly silica-containing components. Additionally, the fire resistance performance improved with increasing coating thickness. Louati et al. [23] successfully synthesized a novel three-dimensional geopolymer material using kaolin and phosphoric acid. They studied the effect of the Si/P molar ratio on the properties of the geopolymer and found that the compressive strength reached its maximum at a Si/P ratio of 2.75. The ductility of geopolymers was also improved by adding Polyvinyl Alcohol (PVA) fibers at a volume fraction of 1.2%, resulting in an increase in flexural strength by 32.91%, 29.8% and 27.3% after 3, 7 and 28 days, respectively. However, the high density remains a challenge for practical applications, as lighter materials are needed to provide thicker fireproof coatings on steel to improve fire resistance [24]. Zhang and Li [25] investigated the adhesive bonding of fire-resistant engineered cementitious composites (FR-ECC) to steel by adding different adhesives to the concrete protective coating. They found that FR-ECC had significantly improved mechanical and adhesive properties compared to conventional spray-applied fire-resistant materials. The addition of acrylic latex improved the FR-ECC matrix/steel interfacial adhesion due to changes in ITZ composition and microstructure.

It can be seen from the preceding discussion that there is a significant research direction focused on reducing the self-weight of cement-based fire-resistant coatings while enhancing their bond strength with steel plates. Fly ash cenosphere (FAC) is a crucial raw material in the development of lightweight concrete, which not only reduces the weight of the material but also offers low thermal conductivity [26, 27]. As such, the addition of FAC is an effective way to reduce the self-weight of fire-resistant materials.

In this study, the ratio of FAC to granulated blast furnace slag (GBFS), the water-to-binder ratio (W/B), and the modulus of the alkaline activator are adjusted to determine the optimal design parameters. Mechanical and thermal tests are performed to assess the performance of the samples. The goal is to design a comprehensive blend of lightweight and highly ductile geopolymer mixture for fire-resistant coatings. The mechanical properties of the fireproof coatings are then evaluated at high temperatures of 300℃, 600℃ and 900℃.To optimize the design parameters of the developed fireproof coating, interface bonding tests are conducted through direct shear, normal shear and tensile tests. The bond strength, damage mechanism, and related microstructure are examined to provide a thorough understanding of the sustainable fireproof coating's performance.

2 Material development and preparation

GBFS is used as the alkali-activated cementitious raw material, and FAC is used as a lightweight filler to reduce self-weight. Table 1 shows the chemical composition of GBFS and FAC (wt.%). A sodium silicate solution is used as the alkali activator. Ratios of the materials were finalized after consulting literature [22] and conducting several lab trials to get desired properties in which 263.4 g of purified water was mixed with 226.0 g of sodium silicate solution (molar ratio $SiO_2/Na_2O = 2.31$, Baume degree 50, content 42%), and then stirred until the solution was diluted. After that, 23.0 g of solid sodium hydroxide was added to the diluted sodium silicate solution, and the mixture was stirred until the solid was fully dissolved. Finally, the solution was sealed with a plastic film in a container and left to stand until it returns to room temperature, at which point the required alkaline activator was prepared.

Table 1. Chemical composition of GBFS and FAC (wt.%)

Compounds	SiO_2	Al_2O_3	Fe_2O_3	CaO	MgO	K_2O	SO_3	Na_2O
GBFS	34.71	19.01	0.70	34.71	9.20	-	0.69	-
FAC	80.59	-	0.036	9.63	0.17	0.01	0.19	8.71

2.1 FAC to GBFS ratio

After mixing ground blast furnace slag (GBFS) with an alkaline activator solution, the mixture hardens rapidly within minutes, making it difficult to mold. Additionally, the ball effect and water absorption effect of fly ash cenosphere (FAC) play a role in the mixture's fluidity. In this set of experiments, the modulus of the alkali activator was maintained at 0.5, and the water to binder (W/B) ratio was kept at 0.5, with 40%, 50%, and 60% of the volume of GBFS being replaced by FAC. The fluidity of the mixture was evaluated using the flow table test method [28] as shown in **Fig. 1**. **Table 2** shows the fluidity values of the samples with different FAC-GBFS ratios. The fluidity of the mixture decreased significantly as the FAC content increased. Every 5% replacement by FAC in volume resulted in a reduction of 1.5-2 cm in flow value. The hollow structure of FAC contains air, which results in reduced thermal conductivity. Through trial-and-error testing, the appropriate ratio of FAC to GBFS was determined to be 0.6:0.4, in line with the design principle of the minimum fluidity limit of 19cm.

Table 2. Flowability test results of samples with varying substitution rates

Mix ID	Volume ratio		Weight (g)		Fluidity value(cm)
	GBFS	FAC	GBFS	FAC	
Mix-A1	70%	30%	1008	161	23.1
Mix-A2	65%	35%	936	149.5	21.4
Mix-A3	60%	40%	864	138	19.5
Mix-A4	55%	45%	792	126.5	18.8
Mix-A5	50%	50%	720	115	16.3

Fig. 1. Flowability test of mixture

2.2 Determination of W/B ratio

The ultimate compressive strength of geopolymers is significantly impacted by water content. In this study, the activator modulus was kept constant at 0.5 and the ratio of FAC to GBFS was maintained at 0.55. The water content was varied by adjusting the W/B ratio, which was set at m(water)/m(binder) = 0.5, 0.55, and 0.6. Six samples with dimensions of 40×40×160 mm were molded for each group. The

samples were then placed in a curing chamber (25℃, 100% humidity) for 28 days. **Table 3** shows the strength results for the samples with varying W/B ratios, demonstrating the significant impact of water content on the ultimate compressive strength of the geopolymer.

Table 3. Strength results of samples with different water-binder ratios

Mix ID	Water-Binder Ratio	Compression strength (MPa)	Flexural strength (MPa)
Mix-B1	0.6	27.3	2.2
Mix-B2	0.55	35.1	5.5
Mix-B3	0.5	36.25	3.6

Table 3 shows a steady improvement in the compressive strength of the samples as the W/B ratio decreases. A reduction in the W/B ratio from 0.6 to 0.55 results in a noticeable increase of 7.8 MPa in compressive strength, whereas a decrease from 0.55 to 0.5 only results in a slight increase of 1.15 MPa. On the other hand, the flexural strength experiences an initial increase from 2.2 MPa to 5.5 MPa as the W/B ratio drops from 0.6 to 0.55, but then drops to 3.6 MPa when the W/B ratio reaches 0.5. This decline in flexural strength can be attributed to the decrease in fluidity which increases the air void content and in turn decreases the flexural strength. After a thorough evaluation, the W/B ratio was set to 0.55 for optimal results.

2.3 Determination of alkali activator modulus

According to a report by Buchwald et al. [29], even a slight variation in the modulus of the alkaline activator can result in substantial changes in its strength development. In this study, the compressive strengths of samples with different alkali activator moduli at the same age were compared by setting the modulus to different gradients (as shown in **Table 4**). The alkali activator mix ratio corresponding to the experimental group with the highest strength was selected to determine the ultimate modulus of the alkali activator modulus.

Table 4. Test parameters of different alkaline activator modulus

Mix ID	Modulus	Activator(g)			Binder(g)	
		$NaSiO_3$	NaOH	Water	GBFS	FAC
Mix-C1	1.2	189.5	27.4	295.5	864	138
Mix-C2	1.4	226.0	23.0	263.4	864	138
Mix-C3	1.6	264.3	18.4	229.8	864	138
Mix-C4	1.8	304.3	13.5	194.6	864	138
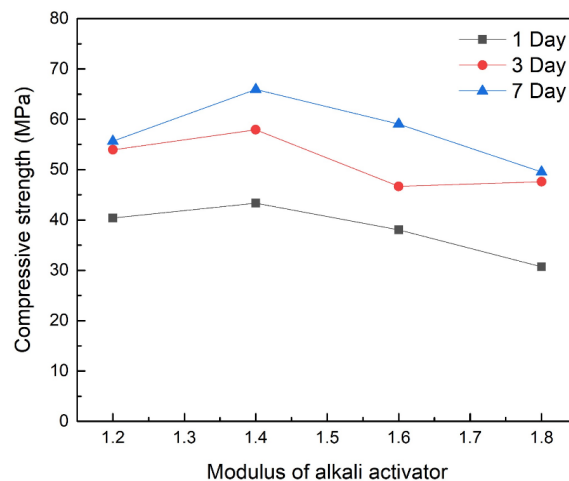
Fig. 2.   Strength comparison of different alkali activator modules at different age

The results of the experiments, as shown in **Fig. 2**, indicate that the strength distribution of the samples with different alkali activator moduli exhibits distinct characteristics at different ages. When the modulus increases from 1.2 to 1.4, the compressive strength of the material exhibits a positive trend. However, when the modulus rises from 1.4 to 1.6, the compressive strength decreases gradually. The

strength of the material reaches its maximum of 65.9 MPa when the modulus is 1.4 and the age is 7 days. It is known that the modulus of sodium silicate represents the ratio of SiO_2 to Na_2O molecules in solution, with a higher modulus indicating a higher content of SiO_2 molecules. Excess SiO_2 molecules prevent the formation of more $Ca_2(Al_2SiO_7)$, while the viscosity of sodium silicate increases with an increasing content of SiO_2 molecules. This makes it difficult to fully stir the reaction mixture, leading to a gradual improvement in strength up to a peak, followed by a decline as the modulus continues to increase.

2.4. Sample preparation process

To ensure an even mix without delamination due to the significant difference in density between FAC and GBFS, the lighter FAC was added first to the bottom of the mixing pot. Then, heavier GBFS was added on top. The pot was mixed at low speed for 2 minutes until the mixture was uniform. The pot was then removed and checked for evenness with a spatula. The pot was returned to its position and the previously prepared alkali solution was added, stirred evenly at high speed for 3 minutes, and checked to prevent sinking. Finally, the mixture was poured into a $40 \times 40 \times 160$ mm mold, producing a self-compacting effect so no vibration was necessary. The mold was covered with plastic wrap to prevent water loss, drying, shrinkage, and cracking. The poured sample was allowed to rest under standard curing conditions for 1 day. Afterwards, the mold was removed, and the sample was placed in a standard curing room (25℃, 100% humidity) to cure for the desired time. Table 5 displays the optimal composition ratio of the geopolymer, which were prepared based on several previously determined parameters.

Table 5. Optimal composition ratio of geopolymer coatings

Alkaline activator(g/L)			Binder(g/L)	
NaSiO$_3$	NaOH	Water	GBFS	FAC
226.0	23.0	263.4	864	138

3. Performance analysis

3.1. High temperature exposure test
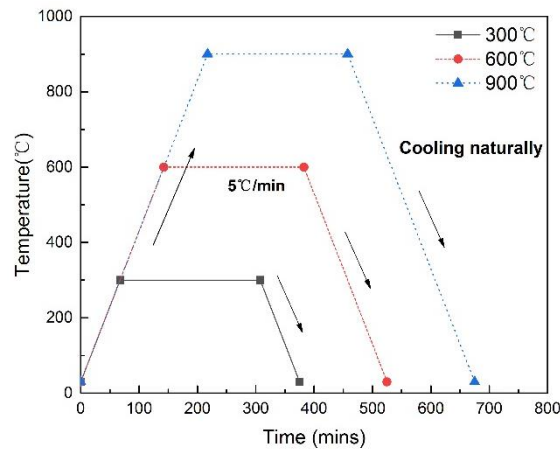
Fig. 3. Heating curves for high temperature exposure test.

The prepared $40 \times 40 \times 160$mm samples were placed in a muffle furnace. In reference to the experimental results by Huang et al. [30,31], the heating rate was limited to 4 ℃/min and the target temperatures were set at 30 ℃, 300 ℃, 600 ℃, and 900 ℃, respectively. After resting at each preset temperature for 4 hours, the samples were naturally cooled to room temperature and the compression and flexural tests were performed immediately afterwards. The specific heating process is shown in **Fig. 3**.

3.2. Interface bonding test

Due to the poor deformation capacity of fire-resistant coatings compared to steel, the fire-resistant material often falls off in advance due to mismatched strains under loading. In order to enhance the bonding between the fire-resistant coating and the steel structure, various measures were attempted in this study to ensure that the fire-resistant material and steel plate perform better when subjected to loads. The bonding interface primarily bears shear and tensile forces. According to the studies of Celik et al. [24] and Yu et al. [32], it can be seen that the addition of fibers can significantly enhance the ductility of cement-based materials. In this study, 1% PE fiber was added to the alkali-activated fire-resistant material to enhance its interaction with the steel plate. To determine the optimal bonding method, commonly referenced bonding methods between fire-resistant materials and steel plates were selected for experiments, as shown in **Table 6**. All the tests were conducted on three samples, and the average values were reported.

Table 6. Bonding techniques between Fire-Resistance coating and steel plate

Label	Coating composition	Interface processing
Fire-resistance material-C	Fire-resistance material	-
Fire-resistance material-S	Fire-resistance material	Adhesive steel
Fire-resistance material-P	Fire-resistance material	PA+cement
Fire-resistance material-PA20	Fire-resistance material+20%PA	-
Fire-resistance material-BA20	Fire-resistance material+20%BA	-

Note*: "20%" represents the mass ratio, "PA" indicates the acrylic emulsion, "BA" denotes the pure acrylic emulsion, "S" refers to the sticky steel glue, and "PA clean paste" is prepared by mixing P O52.5 cement and PA glue at a mass ratio of 1:1.

3.2.1. Direct shear test
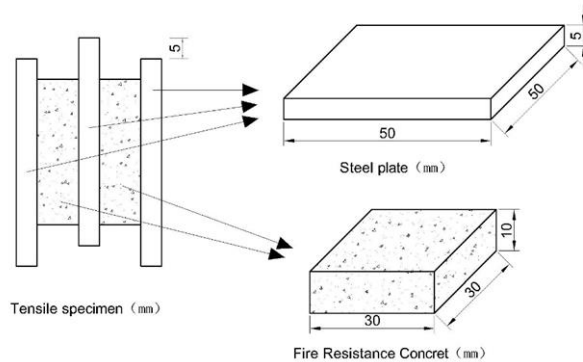
Fig. 4. Sample size for direct shear test.
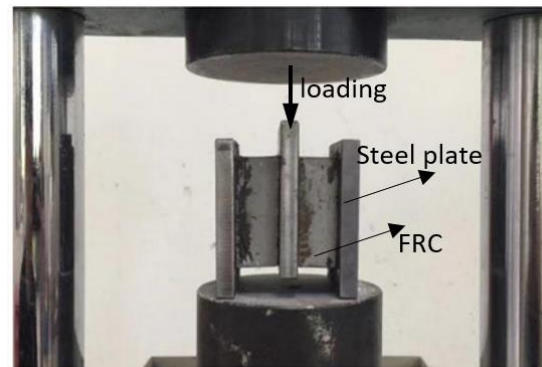
Fig. 5. Shear specimens and test setup.
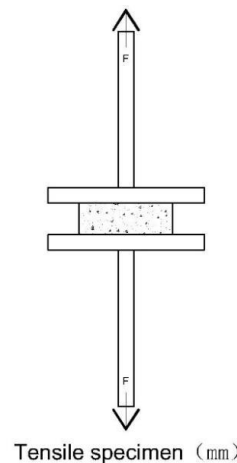
Fig. 6. Tensile test setup and specimen.

Fig. 4 illustrates the dimensions of each part of the sample used for the direct shear test. The middle part and both sides of the test piece consist of steel plates, with a fire-resistance material sandwiched in between. When subjected to loading, the steel plates on both sides provide support, while the middle steel plate is subjected to compression to evaluate the bonding performance of the fire-resistance material at the interface between the two sides of the middle steel plate at the rate of 0.5 mm/min. The shear specimen and the setup for the shear test are depicted in **Fig. 5**.

3.2.2. Normal shear test

The middle portion of the sample used in the tensile test consists of fire-resistance material with a pair of T-shaped steel plates bonded to the upper and lower portions. The normal pull-out bonding performance of the interface between the steel plate and fire-resistance material is tested by applying a load vertically from the top at the rate of 0.5 mm/min. **Fig. 6** shows the tensile test setup and specimen.

3.2.3. Tensile test of fire-resistive material coated steel

The prepared test pieces, based on the experimental parameters determined in Section 2, were used to study the failure mechanism of the fire-resistant material coated steel under tensile load. **Fig. 7** shows the size of the steel plate, strain gauge layout and the fire-resistant material coated steel sample. During the test, the sample was pulled vertically at a rate of 0.4 mm/min and the strain was recorded at an acquisition rate of 1Hz and a sample rate of 100Hz. A 5mm length strain gauge was used for the steel plate with an effective strain range of 2%, and a 30mm length strain gauge was used for the fire-resistant material with an effective range of 4.5%.
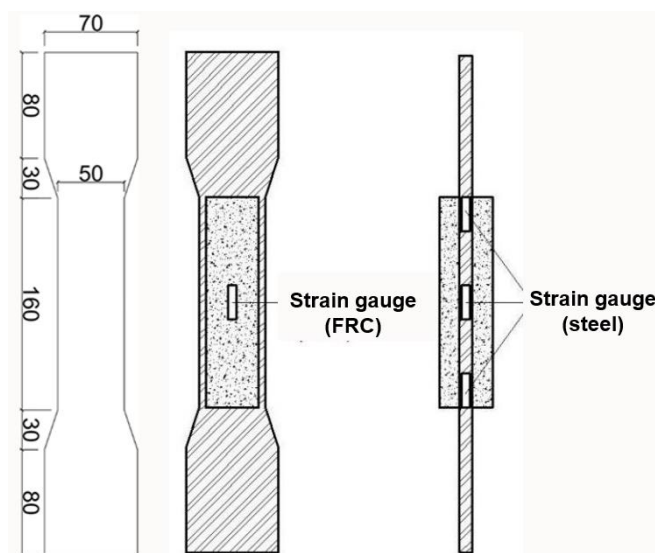
Fig. 7. Size, strain gauge layout and schematic diagram of the fireproofing coated steel plate.

3.3 X-Ray Diffraction (XRD)

XRD was conducted to identify the crystalline phases in the fireproofing coatings subjected to different temperatures (30 ℃, 300 ℃, 600 ℃, and 900 ℃). XRD tests were conducted by using a diffractometer which was equipped with a D/teX Ultra 250 1D detector. It used a Bragg-Brentano vertical θ-θ geometry in θ-2θ pattern. Powdered samples (<45 μm) were prepared, and the readings were taken continuously at a scanning speed of 2 °/min with step size of 0.02° 2θ, for the range of 5–70° 2θ. The machine was operated at voltage of 40 kV and current 30 mA, using CuKα radiation (λKα1 = 1.5406 Å and λKα2 = 1.5444 Å).

3.3 Scanning Electron Microscopy (SEM)

SEM analysis was carried out to examine the microstructure and morphology of the fireproofing coatings. After 28 days of curing in water, small sections of the samples were first cleaned and dried, followed by application of a thin layer of gold. The prepared sample was then inserted in the machine.

The morphologies were captured at different magnifications between 10 μm to 200 μm at an accelerating voltage of 10 and 15 kV.

4. Results and discussion

4.1. High temperature exposure test

Fig. 9 presents the surface morphology of the fire-resistant material after being heated at temperatures of 30, 300, 600, and 900℃. In Fig. 9(a), the control group at room temperature (30℃) is shown to have a typical greenish color and a dense texture without cracks, with a slight white Ca(OH)$_2$ crystal frost visible on the surface. Fig. 9(b) depicts the sample after being heated at 300℃, displaying a grayish-white color with a few linear cracks present. In Fig. 9(c), the sample after being heated at 600℃ shows an increase in the number of cracks, with the width of the cracks remaining unchanged and the shape shifting from linear to zigzag. Fig. 9(d) shows the surface morphology after heating at 900℃, with further increased numbers and widths of cracks, but still intact without any signs of disintegration or shedding.

(a)30℃　　　　　(b)300℃　　　　　(c)600℃　　　　　(d)900℃
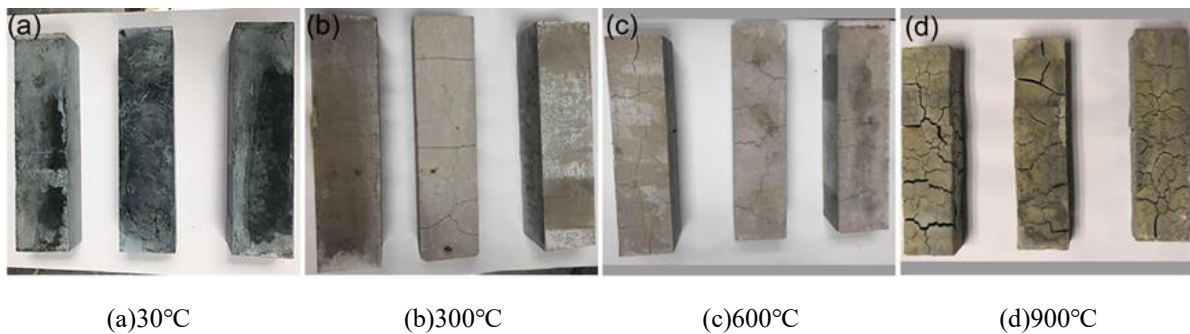
Fig. 9. Surface morphology of fire-resistance material after being heated at temperatures of: 30℃, 300℃, 600℃, 900℃.

4.1.1. XRD analysis
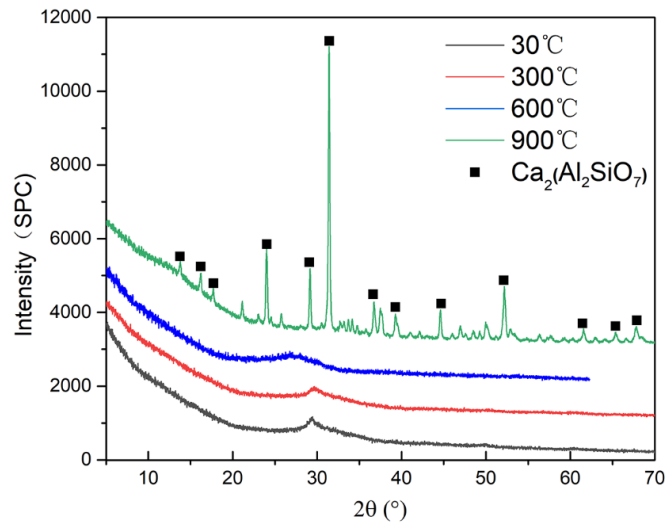
Fig. 10. X-ray diffraction patterns of fire-resistance geopolymer at 30, 300, 600℃ and 900℃.

The XRD diffraction pattern in Fig. 10 shows a clear hump in the fire-resistant material at 30, 300, and 600℃, indicating that the material is a typical Ca$_2$(Al$_2$SiO$_7$) in gel state [28]. At 900℃, new crystalline substances are generated, as evidenced by the appearance of additional diffraction peaks, though the analysis shows that it remains Ca$_2$(Al$_2$SiO$_7$). At this temperature, the Ca$_2$(Al$_2$SiO$_7$) in gel state undergoes dehydration and transforms into crystalline Ca$_2$(Al$_2$SiO$_7$), affecting the strength of the geopolymer. According to Strum et al. [33], the crystalline form of Ca$_2$(Al$_2$SiO$_7$) is referred to as zeolite, which has a loose and porous structure with high porosity. As the temperature increases, more zeolite

is generated, causing the material to become more porous and its strength to decline. However, the porous structure of zeolite also improves the material's thermal insulation performance. As a result, the higher the temperature, the better the thermal insulation performance of the material. Temuujin et al. [22] obtained geopolymer samples through alkali-activation of fly ash and found that after 1 hour of heating at 1000 ℃, the geopolymer remained basically amorphous without undergoing any phase changes. The reduction in strength can be reversed by adding a suitable amount of fly ash, which can also enhance the material's thermal insulation properties.

4.1.2. SEM analysis
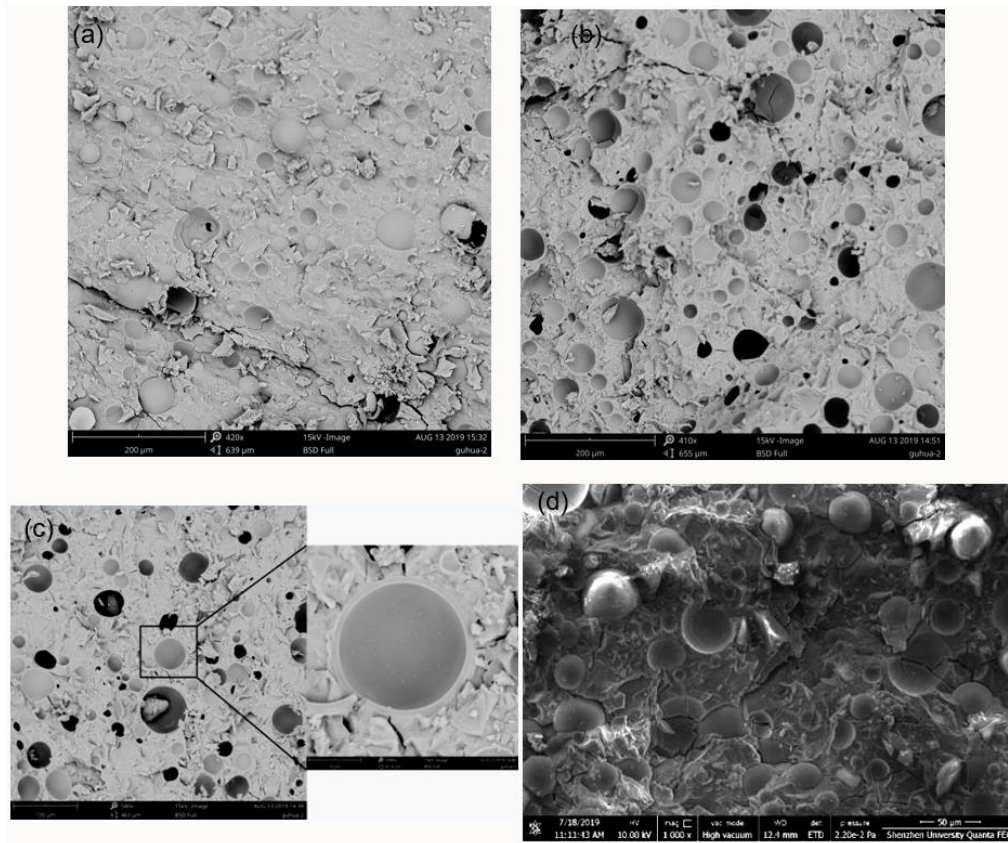
Fig. 11.   Geopolymer microstructure (a) 30 ℃, (b) 300 ℃, (c) 600 ℃, (d) 900 ℃.
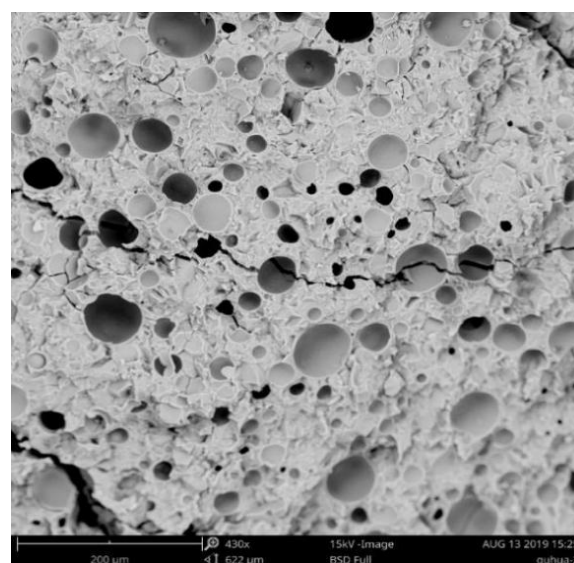
Fig. 12.   The path of development when cracks occur inside the matrix at 600℃.

Fig. 11 illustrates the microstructure of the geopolymer after exposure to different temperatures. In **Fig. 11**(c), an enlarged view of the FAC (Fine Alumina Calcium) and the surrounding matrix is shown. It can be observed that FAC is not dissolved in a highly alkaline environment and is evenly distributed in the fire-resistant material. The matrix is dense and free of bubbles, with the light and dark circles representing different sizes of FAC. Some of the particles and flakes are remnants from the sample's destruction process. The enlarged view reveals that the sample's fracture surface is smooth, the interface between the matrix and FAC is tightly combined, and there is no peeling between the two. **Fig. 12** depicts the internal crack progression in the sample matrix at 600 ℃. As shown, the bonding surface of FAC and geopolymer remains strong under stress, with no cracks extending along the interface between FAC and the matrix. Instead, the cracks continue through FAC, indicating a joint contribution from both FAC and geopolymer in sustaining external forces. **Fig. 13** compares the local micro-morphology of the geopolymer at 30 °and 600 ℃. By comparing the electron microscope images, it can be seen that the pores in the geopolymer matrix significantly increase as the temperature rises, transforming from a dense to porous structure. This aligns with the results of XRD diffraction pattern analysis, which suggest that the gel state $Ca_2(Al_2SiO_7)$ transforms into porous crystalline zeolite as the temperature increases. This leads to a decrease in the material's strength and improves its thermal insulation properties.

(a) 30℃   (b) 600℃
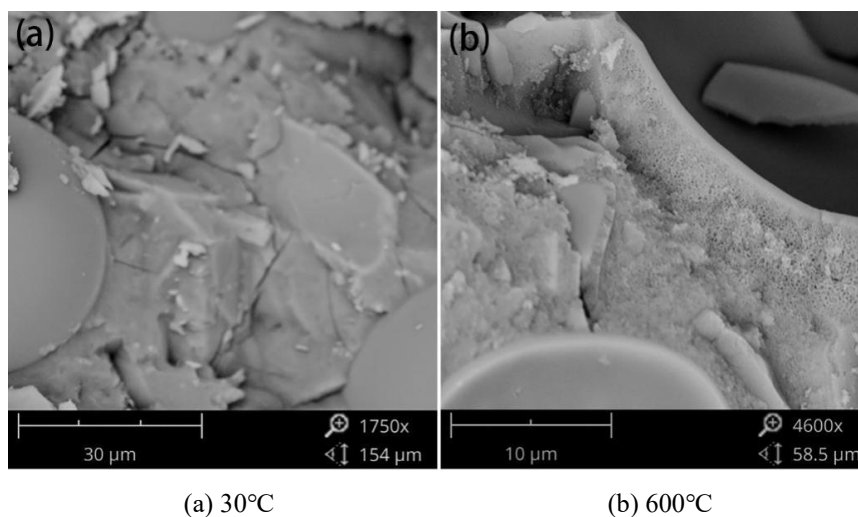
Fig. 13.   Local micro-morphology of the geopolymer.

4.1.3. Compression and flexural strength

Fig. 14 displays the compressive and flexural strength curves of the fire-resistant material after being subjected to various temperatures and then cooled to room temperature. As depicted, the compressive and flexural strengths both decline with increasing temperature. At 600 ℃, the compressive strength retains 71.4% of its strength at room temperature, and the flexural strength retains 62.5% of its strength at room temperature. However, at 900 ℃, the decrease in strength occurs more rapidly, with the compressive strength retaining 31.7% and the flexural strength retaining 30.2% of their respective strengths at room temperature. **Fig. 15** depicts the failure mode of the fire-resistant geopolymer after exposure to different temperatures and subsequent cooling to room temperature. It can be seen that the sample exhibits a typical X shape after compression testing, indicating that the material retains load-bearing capability despite visible macro cracks on the surface. The XRD and SEM results reveal that, from 30 to 600 ℃, the dominant component inside the material remains gel calcium aluminosilicate and there is no significant change in the internal structure. The decrease in compressive and flexural strength at this stage is primarily due to surface crack extension. Between 600 and 900 ℃, the main component transforms from gel calcium aluminosilicate to zeolite and the microstructure shifts from dense to porous, leading to a rapid decrease in strength due to both internal and external factors. **Fig. 16** presents a comparison of the residual strength of the geopolymer fire-resistant material to that of other fire-resistant materials of the same type. It is clear that, compared to other inorganic fire-resistant materials, the geopolymer fire-resistant material developed in this study exhibits higher residual strength across

various temperatures [30, 31, 34].

(a) Compressive strength (b) Flexural strength
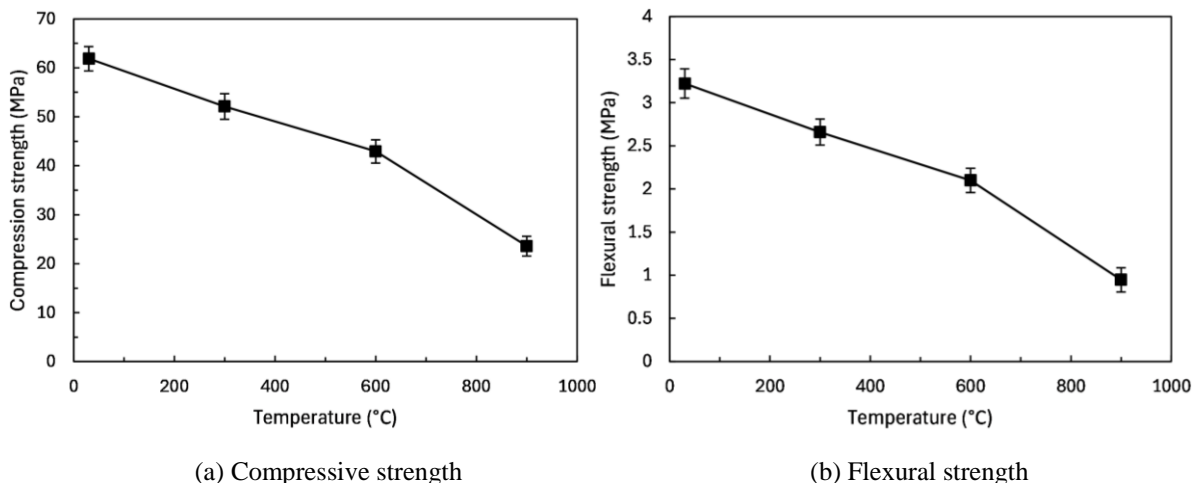
Fig. 14. Compressive and flexural strength of fireproofing coatings after exposed at 30, 300, 600 and 900℃.

(a) 30℃ (b)300℃, 600℃ (c)900℃
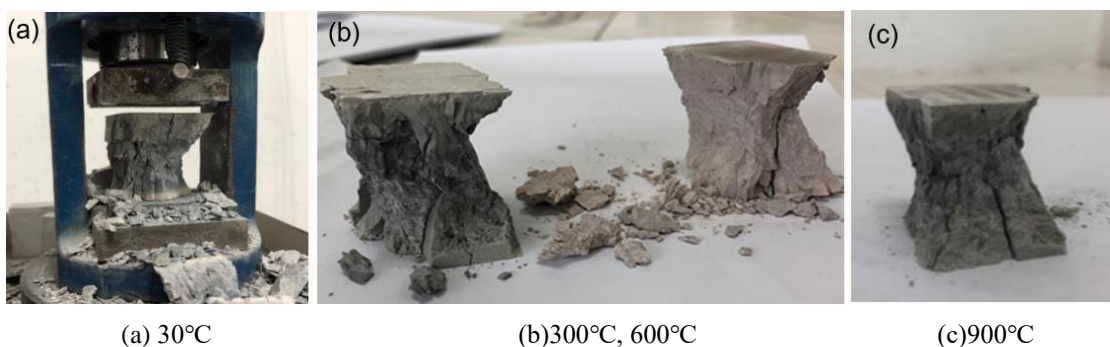
Fig. 15. Failure model of fire-resistance geopolymer after exposed at 30℃, 300℃, 600℃ and 900℃.
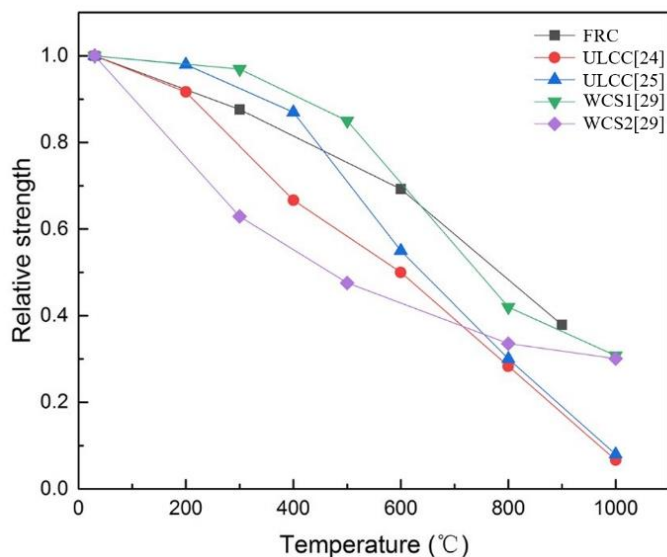
Fig. 16. Comparison of residual strength of geopolymer fire-resistance material with other fire-resistance materials.

4.2. Analysis of interface bond

4.2.1. Bond strength of normal and direct shear

Table 7 presents the average test results of three samples of the strength and mode of failure of different bonding methods. In the fire-resistant material-PA20 and fire-resistant material-BA20 (20% PA glue and BA glue added), the bonding strength between the fire-resistant material and steel plate improved to 0.12 MPa and 0.11 MPa, respectively, from 0.07 MPa. The results show that the increase in shear and normal tensile strength is minimal due to poor bonding between the fire-resistant material and the steel plate, making it unsuitable as a replacement for the interface adhesive. **Fig. 17(a)** and **Fig. 17(b)** show the failure mode of fire-resistance material to steel interface. In the event of failure, the bonding interface fails before the fire-resistant material and the fire-resistant material detaches. When subjected to tensile force, the fire-resistant material-S and fire-resistant material-P (PA+cement, cement-steel bonding) fail before the bonding interface, meeting the requirements for actual use. However, using PA glue in a humid environment accelerates steel corrosion, as shown in **Fig. 17(c)**, making it unsuitable as an interface adhesive. The shear bond strength and normal bond strength of fire-resistant material-S are significantly higher compared to PA glue and BA glue, with the normal bond strength and shear bond strength 119% and 205% higher, respectively. The mode of failure is cohesive failure of the fire-resistant material before the bonding interface. Based on the experimental results, the fire-resistant material-S bonding method is the optimal choice.

Table 7. Strength and failure modes with different bonding technique

Strength (MPa)	Fire-resistance material-C	Fire-resistance material-S	Fire-resistance material-P	Fire-resistance material-PA20	Fire-resistance material-BA20
Normal shear	0.07	1.43 (Fire-resistance material failure)	1.41 (Fire-resistance material failure)（Rust）	0.12	0.11
Direct shear	0.05	1.64 (Fire-resistance material failure)	– （Rust）	0.08	0.07

(a) fire-resistance material-BA20　　(b) fire-resistance material-P　　(c) fire-resistance material-P

Fig. 17. Failure mode.

4.2.1.1 Cohesive Properties of Fire-resistant Material-S

Fire-resistant material-S, which uses sticky steel glue as an adhesive, shows superior bond strength due to the high adhesion properties of the steel glue. The cohesive failure observed suggests that the adhesive itself is robust, making it a suitable choice for enhancing the bonding interface between the fire-resistant material and the steel plate.

4.2.1.2 Surface Preparation and Chemical Compatibility

Proper surface preparation, including cleaning and roughening, significantly enhances the mechanical interlocking and chemical bonding at the interface. Adhesive steel, used in fire-resistant material-S, ensures better adhesion due to its compatibility with both the fire-resistant material and the steel substrate.

4.2.1.3 Mechanical Interlocking Effect

The incorporation of 1% PE fiber into the alkali-activated fire-resistant material improved the mechanical interlocking at the interface, enhancing bond strength and ductility. This fiber addition

helped to distribute the stress more evenly and prevents premature detachment.

4.2.1.4 Role of Cement in Fire-resistant Material-P

The PA+cement combination in fire-resistant material-P provides a dual bonding mechanism. The PA glue enhances adhesion while the cement provides a dense microstructure that contributes to the overall strength and stability of the bond. However, the presence of PA glue can lead to corrosion in humid environments, as noted with rust observations.

4.2.2. Tensile test of coated steel plate
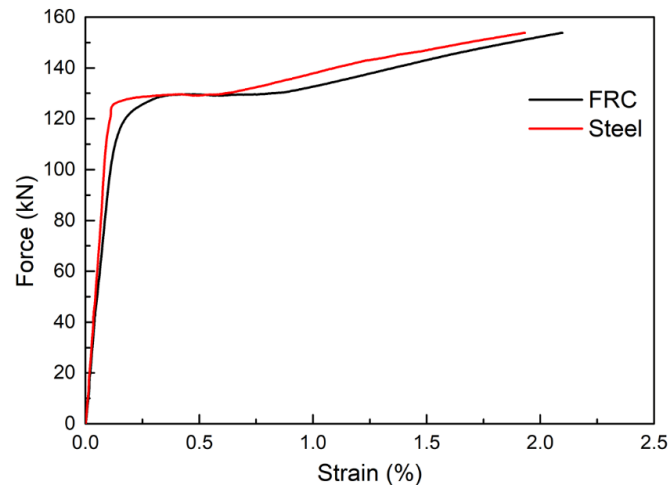
Fig. 18.   Load-strain curve between fire-resistance material and steel.
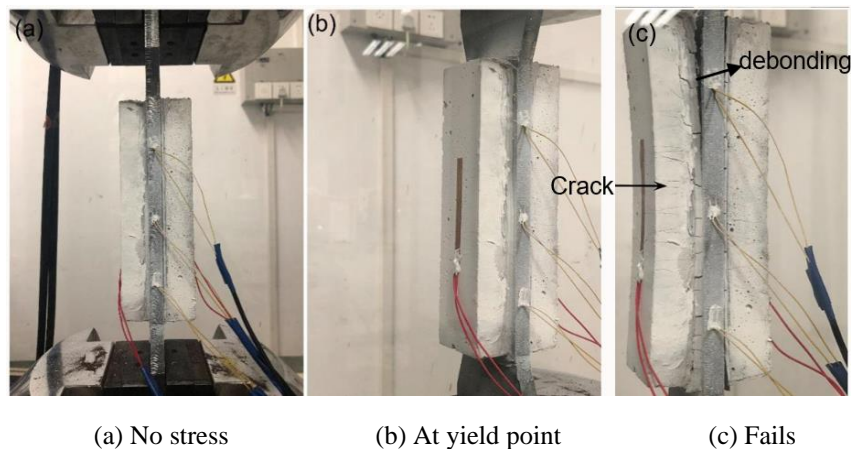
(a) No stress   (b) At yield point   (c) Fails

Fig. 19.   Specimen in the test.

Fig. 18 displays the average force-strain curves of the fire-resistant material and steel, obtained through the testing of three specimens. As seen in the figure, the force-strain curves of the steel plate and the fire-resistant material generally coincide, indicating a joint contribution to strain coordination and a satisfactory bonding effect. **Fig. 19** depicts the state of the specimen at various stages of stress. **Fig. 19**(a) shows that the fire-resistant material and steel plate are fully bonded at the start of the experiment. **Fig. 19**(b) reveals the state of the specimen when the steel plate reaches its yield strength, and it is apparent that the fire-resistant material and steel plate remain well bonded with no visible cracks at the bonding interface. At this point, the fire-resistant material has a strain of about 0.5%, with only a few small cracks on the surface, which extend from the bonding interface to the thickness of the fire-resistant material. **Fig. 19**(c) shows that the end of the fire-resistant material has lifted, and the strain gauge has failed, with the middle of the fire-resistant material now reaching a strain of over 4% and expanding in multiple cracks from the bonding interface to the thickness direction. However, due

to poor ductility of the steel adhesive, fracture occurs. The two ends of the fire-resistant material are then released from constraint and become more highly stressed, causing the material to separate from the steel plate. After separation, the two ends are bounced back towards the middle by the fiber connection, and the gradual extension to the middle continues as the strain increases. The test results demonstrate that the composite action ability of the steel plate and fire-resistant material is improved when the newly developed fire-resistant material is bonded to the steel plate, leading to consistent strain at each deformation stage and preventing detachment and failure.

The interface bonding mechanism between the fire-resistant coating and the steel plate can be attributed to both mechanical interlocking and chemical bonding. Mechanical interlocking occurs due to the roughness of the steel surface and the penetration of the adhesive into the micro-roughness, creating a physical bond. Chemical bonding results from the interaction between the adhesive components and the steel surface, forming strong chemical bonds at the interface.

5. Conclusion

In this study, a novel sustainable lightweight and high ductility geopolymer-based fire-resistant material was developed using fly ash and granulated blast furnace slag. The high temperature fire resistance properties of this material were tested, and its ductility bond strength was improved by adding polyethylene fiber and selecting a suitable bonding method. The interface bonding performance was evaluated through direct shear, normal shear, and tensile tests of the fire-resistant material coated steel plate. The following conclusions were drawn:

(1) When the ratio of fly ash to granulated blast furnace slag was 0.6:0.4, the water-to-binder ratio was 0.55, and the alkali activator modulus was 1.4, the geopolymer demonstrated its lightweight characteristic (density of $1.4 g/cm^3$) and maintained around 30% of its room temperature strength (compressive strength of 23 MPa, flexural strength of 0.9 MPa) even at a high temperature of 900℃.

(2) During the high-temperature test, the fire-resistant material surface exhibited cracks that increased in number and width as the temperature increased. However, at 900℃, the sample remained intact and showed no signs of disintegration or shedding.

(3) At temperatures of 30, 300, and 600℃, the geopolymers were in a gel-like state, represented by the compound $Ca_2(Al_2SiO_7)$. At 900 ℃, the gel-like $Ca_2(Al_2SiO_7)$ underwent gradual dehydration and transformed into the crystalline zeolite $Ca_2(Al_2SiO_7)$ with high porosity.

(4) As the load increased, the modified fire-resistant material, characterized by multi-crack expansion, deformed in conjunction with the steel plate. During the elastic deformation stage of the steel plate, the maximum strain of the high ductility fire-resistant material reached 4%, demonstrating its high ductility and excellent anti-stripping properties.

CRediT authorship contribution statement

Zhenyu Huang: Conceptualization, Funding acquisition, Supervision, Investigation, Formal analysis, Writing – original draft. **Yingwu Zhou:** Formal analysis, review and editing. **Hammad Salahuddin:** Formal analysis, Writing, review and editing.

Conflicts of Interest

The authors declare that they have no conflicts of interest to report regarding the present study.

References

[1]   Wu Y, Xu Y, Shi Y, Ban H. Overall buckling behavior of fire-resistant steel welded I-section columns under ambient temperature. J Constr Steel Res. 2019; 157(6): 32-45. doi: 10.1016/j.jcsr.2019.02.019

[2]   Nikmatin S, Hermawan B, Sukardan D, Irmansyah I, Suhartono S, Syafiuddin A. Enhancement of physical, chemical, and mechanical properties of biocomposite for the fire resistant material application. Biointerface Res Appl Chem. 2020; 10(3): 5423-5428. doi: 10.33263/BRIAC103.423428

[3]   Wang Y, Liu F, Yang H, Fu F, Yan Y. Thermal insulation performance of non-load-bearing light gauge slotted steel stud walls. Sustainable Structures, 2024; 4(1): 000042. doi: 10.54113/j.sust.2024.000042.

[4]   Qiao C, Pan Q, Zhang Z, Hu P. Research on Component Recycling Based on Steel Structure Prefabricated Building. In: IOP Conference Series: Earth and Environmental Science 2019; 330(2): 022079. doi: 10.1088/1755-1315/330/2/022079

[5]   Yu C, Tong J, Zhou S, Zhang J, Shen J, Zhang L, Tong G, Li Q, Xu S. State-of-the-art review on steel-concrete composite walls. Sustainable Structures, 2024; 4(1): 000035. doi: 10.54113/j.sust.2024.000035.

[6]   Korkmaz KA, Uzer M. Seismic Behavior Investigation of Prefabricated Steel Industrial Buildings. Key Eng Mater 2018; 763(5): 131-138 KEM. doi:10.4028/www.scientific.net/KEM.763.131

[7]   Xie T, Fang C. Nanomaterials Applied in Modifications of Geopolymer Composites: a Review. Australian Journal of Civil Engineering. 2019; 17(1): 32-49. doi: 10.1080/14488353.2019.1614353

[8]   Davidovits J. Geopolymers : inorganic polymeric new materials. Journal of Thermal Analysis. 1991;37(8) :1633-1656. doi: 10.1007/bf01912193

[9]   Yong HC, Ming LY, Al Bakri Abdullah MM, Hussin K. Fire resistant properties of geopolymers: A review. In: Key Engineering Materials. 2015; 660(20): 39-43. doi: 10.4028/www.scientific.net/KEM.660.39

[10]   Provis JL, van Deventer JSJ. Geopolymerisation kinetics. 1. In situ energy-dispersive X-ray diffractometry. Chem Eng Sci. 2007; 62(9): 2309-2317. doi: 10.1016/j.ces.2007.01.027

[11]   Tennakoon C, Shayan A, Sanjayan JG, Xu A. Chloride ingress and steel corrosion in geopolymer concrete based on long term tests. Mater Des. 2017; 116(4): 287-299 doi: 10.1016/j.matdes.2016.12.030

[12]   Sufian Badar M, Kupwade-Patil K, Bernal SA, Provis JL, Allouche EN. Corrosion of steel bars induced by accelerated carbonation in low and high calcium fly ash geopolymer concretes. Constr Build Mater. 2014; 61(12): 79-89. doi: 10.1016/j.conbuildmat.2014.03.015

[13]   Kriven WM, Gordon M, Ervin BL, Reis H. Corrosion Protection Assessment of Concrete Reinforcing Bars with a Geopolymer Coating. In: Developments in Porous, Biological and Geopolymer Ceramics. 2009; 28(9): 373-381. doi: 10.1002/9780470339749.ch33

[14]   Aliabdo AA, Abd Elmoaty AEM, Mohamed MF. Permeability indices and corrosion resistance of geopolymer and Portland cement concretes. Magazine of Concrete Research. 2018; 70(12): 595-609. doi: 10.1680/jmacr.17.00151

[15]   Nguyen KT, Le TA, Lee K. Evaluation of the mechanical properties of sea sand-based geopolymer concrete and the corrosion of embedded steel bar. Constr Build Mater. 2018; 169(12): 462-472. doi: 10.1016/j.conbuildmat.2018.02.169

[16]   Davidovits J. Geopolymers and geopolymeric materials. Journal of Thermal Analysis. 1989; 35(2): 429-441. doi: 10.1007/bf01904446

[17]   Lassinantti Gualtieri M, Romagnoli M, Gualtieri AF. Preparation of phosphoric acid-based geopolymer foams using limestone as pore forming agent - Thermal properties by in situ XRPD and Rietveld refinements. J Eur Ceram Soc. 2015; 35(11): 3167-3178. doi: 10.1016/j.jeurceramsoc.2015.04.030

[18]   Vaou V, Panias D. Thermal insulating foamy geopolymers from perlite. Miner Eng. 2010; 23(14): 1146-1151. doi: 10.1016/j.mineng.2010.07.015

[19]   Bai C, Franchin G, Elsayed H, et al. High-porosity geopolymer foams with tailored porosity for thermal insulation and wastewater treatment. J Mater Res. 2017; 32(17): 3251-3259. doi: 10.1557/jmr.2017.127

[20]   Samson G, Cyr M, Gao XX. Thermomechanical performance of blended metakaolin-GGBS alkali-activated foam concrete. Constr Build Mater. 2017; 157(28): 982-993. doi: 10.1016/j.conbuildmat.2017.09.146

[21]   Peng K Di, Zeng JJ, Huang BT, Huang JQ, Zhuge Y, Dai JG. Bond performance of FRP bars in plain and fiber-reinforced geopolymer under pull-out loading. Journal of Building Engineering. 2022; 57(13): 1-17. doi: 10.1016/j.jobe.2022.104893

[22]   Temuujin J, Minjigmaa A, Rickard W, Lee M, Williams I, van Riessen A. Fly ash based geopolymer thin coatings on metal substrates and its thermal evaluation. J Hazard Mater. 2010; 180(1-3): 748-752. doi: 10.1016/j.jhazmat.2010.04.121

[23]   Louati S, Baklouti S, Samet B. Geopolymers Based on Phosphoric Acid and Illito-Kaolinitic Clay. Advances in Materials Science and Engineering. 2016; 2016(1): 1-7. doi: 10.1155/2016/2359759

[24]   Celik A, Yilmaz K, Canpolat O, Al-mashhadani MM, Aygörmez Y, Uysal M. High-temperature behavior and mechanical characteristics of boron waste additive metakaolin based geopolymer composites reinforced with synthetic fibers. Constr Build Mater. 2018; 187(30): 1190-1203. doi: 10.1016/j.conbuildmat.2018.08.062

[25] Zhang Q, Li VC. Adhesive bonding of fire-resistive engineered cementitious composites (ECC) to steel. Constr Build Mater. 2014; 64(15): 431-439. doi: 10.1016/j.conbuildmat.2014.04.059

[26] Baidzhanov D, Nuguzhinov Z, Fedorchenko V, Divak L. Heat Insulation Materials Based on Cenospheres. Applied Mechanics and Materials. 2015; 725-726(3): 383-390. doi: 10.4028/www.scientific.net/amm.725-726.383

[27] Deepthi M V., Sharma M, Sailaja RRN, Anantha P, Sampathkumaran P, Seetharamu S. Mechanical and thermal characteristics of high density polyethylene-fly ash Cenospheres composites. Mater Des. 2010; 31(4): 2051-2060. doi: 10.1016/j.matdes.2009.10.014

[28] British Standards Institution. BS EN 1015-3:1999 Methods of Test for Mortar for Masonry - Part 3 : Determination of Consistence of Fresh Mortar (by Flow Table). 2004; 3.   doi: 10.3403/01541440

[29] Buchwald A, Zellmann HD, Kaps C. Condensation of aluminosilicate gels-model system for geopolymer binders. J Non Cryst Solids. 2011; 357(5): 1376-1382. doi: 10.1016/j.jnoncrysol.2010.12.036

[30] Huang Z, Liew JYR, Li W. Evaluation of compressive behavior of ultra-lightweight cement composite after elevated temperature exposure. Constr Build Mater. 2017; 148(19): 579-589. doi: 10.1016/j.conbuildmat.2017.04.121

[31] Huang Z, Padmaja K, Li S, Liew JYR. Mechanical properties and microstructure of ultra-lightweight cement composites with fly ash cenospheres after exposure to high temperatures. Constr Build Mater. 2018; 164(7): 760-774. doi: 10.1016/j.conbuildmat.2018.01.009

[32] Yu K, Wang Y, Yu J, Xu S. A strain-hardening cementitious composites with the tensile capacity up to 8%. Constr Build Mater. 2017; 137(8): 410-419. doi: 10.1016/j.conbuildmat.2017.01.060

[33] Sturm P, Gluth GJG, Simon S, Brouwers HJH, Kühne HC. The effect of heat treatment on the mechanical and structural properties of one-part geopolymer-zeolite composites. Thermochim Acta. 2016; 635(11): 41-58. doi: 10.1016/j.tca.2016.04.015

[34] Abdel-Ghani NT, Elsayed HA, Abdel Moied S. Geopolymer synthesis by the alkali-activation of blast furnace steel slag and its fire-resistance. Hbrc Journal. 2018; 14(2): 159-164. doi: 10.1016/j.hbrcj.2016.06.001